Available online at www.sciencedirect.com

jmr&t Journal of Materials Research and Technology

journal homepage: www.elsevier.com/locate/jmrt

Original Article

Correlative cross-sectional characterization of nitrided, carburized and shot-peened steels: synchrotron micro-X-ray diffraction analysis of stress, microstructure and phase gradients

S.C. Bodner [a,*], M. Meindlhumer [b], T. Ziegelwanger [a], H. Winklmayr [c], T. Hatzenbichler [c], C. Schindelbacher [c], B. Sartory [d], M. Krobath [d], W. Ecker [d], N. Schell [e], J. Keckes [a]

[a] Department Materials Science, Chair of Materials Physics, Montanuniversität Leoben, Jahnstraße 12, Leoben, Styria, 8700, Austria

[b] Department Materials Science, Christian Doppler Laboratory for Advanced Synthesis of Novel Multifunctional Coatings, Montanuniversität Leoben, Roseggerstraße 12, Leoben, Styria, 8700, Austria

[c] Pankl Racing Systems AG, Kapfenberg, Styria, 8610, Austria

[d] Materials Center Leoben, Roseggerstraße 15, Leoben, Styria, 8700, Austria

[e] Helmholtz Zentrum Geesthacht, Institute of Materials Research, GEMS, Notkestraße 85, Hamburg, 22607, Germany

ARTICLE INFO

Article history:
Received 6 September 2020
Accepted 26 January 2021
Available online 3 February 2021

Keywords:
Cross-section analysis
Synchrotron micro-XRD
Near-surface characterization
Case-hardening
Low-pressure-plasma nitriding
Shot-peening

ABSTRACT

Mechanical properties of case modified steels depend decisively on the near-surface gradients of residual stresses, microstructures, phases and chemical composition, which are generated by the empirically well-established case-hardening techniques. Currently, however, to obtain the correlation between near-surface structure–property gradients, applied hardening process parameters and steels' overall performance is a very challenging task. In this work, high-energy synchrotron cross-sectional X-ray diffraction (CSmicroXRD) using a pencil beam cross-section of 20 × 500 μm^2 and complementary analytical techniques are used to characterize the surface-to-bulk gradient of (i) a plasma nitrided steel W300, (ii) a carburized case hardening steel (grade 18CrNiMo7-6) and (iii) a shot-peened high strength steel, type 300M. CSmicroXRD analysis reveals complex gradients of martensite and austenite phases, residual stresses in both phases, crystallographic texture and the evolution of diffraction peak broadening with a spatial resolution of ~20 μm. These parameters are correlated with the gradients of hardness, morphology-microstructure and with the changes in N and C concentrations and/or retained austenite formation/depletion in all three model samples. Finally, the correlative micro-analytics approach indicates the complexity of near surface structure-property relationships as well as the importance of innovative cross-sectional characterization, which

* Corresponding author.
E-mail address: sabine.bodner@unileoben.ac.at (S.C. Bodner).

https://doi.org/10.1016/j.jmrt.2021.01.099

allows for assessing gradual near-surface physical and/or chemical changes accompanying thermo-chemical and mechanical surface treatments.

1. Introduction

Advanced thermo-chemical surface treatments have been used to increase the mechanical performance of steel parts such as cam or ring gear, automotive components, drills and valves [1]. They provide these parts with a hard case and a tough core resulting in adequate fatigue strength and wear resistance, respectively, preventing brittle failure under high impact loads. Resulting functional aspects relevant to the industrial applications are in particular weight reductions due to topology optimization and/or an extended service life. Especially case-hardening technologies such as nitriding, carburizing, boronizing, nitrocarburizing and carbonitriding enhance the tooth root bending strength in gear components [2], the resistance against tensile and impact loads as well as alternating bending fatigue loading. Additional benefits are minimized distortion of the components due to the adaption of the residual stress state, the formation of microstructure depth gradients and the enhancement of corrosion and wear resistance in iron-based alloys [3,4].

Another possibility to enhance the mechanical properties of steels are mechanical surface modifications, like shot peening, which can even be applied to priorly thermally or thermo-chemically treated steels [5–7]. The surface plastification and work hardening is accompanied by the formation of compressive stress gradients, which favourably influence the fatigue resistance [8,9].

The common nitriding, carburizing and shot-peening treatments result in the formation of complex near surface depth gradients of microstructure, chemical composition, residual stress and/or crystalline phases, which, together with the alloying concept, decisively influence steel parts' mechanical properties. Currently, however, it is not trivial to correlate the applied surface treatment process parameters, the fabricated near-surface gradients and the parts' mechanical behaviour. The impact of the treatments at the micro, meso- and macroscale are usually assessed by (micro) hardness depth profiling [2,6,10], nanoindentation, optical and scanning electron microscopies (OM, SEM) and electron probe microanalysis [11]. In order to characterize microstructure, phase and stress gradients, X-ray and neutron diffraction [2,3,12] have been routinely applied (i) by analysing successively etched sample surfaces [13] and/or (ii) by using advanced grazing-incidence diffraction geometries, which require an inverse *Laplace transformation* of the data [14]. However, these techniques operating in *reflection diffraction geometries* provide structural data averaged across the respective X-ray or neutron beam penetration depths and their interpretation is therefore not always unambiguous [14–16].

A further development of the surface treatment technologies requires a comprehensive understanding of physical and chemical near-surface changes that take place during the process with highest possible depth-resolution. The above mentioned surface treatments and corresponding recipes have been developed and used for decades. Although chemical gradients can nowadays be resolved on a nanoscale, there are several diffusion-induced phenomena within the parts' surfaces that have not been fully understood yet. These specifically include the incremental evolution and stabilization of phase gradients and their corresponding distributions of residual stresses as well as the microstructure within the individual phases, like in martensite and austenite [15,17].

This work focusses on the correlative cross-sectional characterization of exemplary (i) a low-pressure plasma nitrided hot-working steel, (ii) a low-pressure carburized case-hardening steel, and (iii) a shot-peened high performance steel grade. Results obtained from conventional laboratory experiments (OM, SEM, hardness profiling, electron microprobe analysis) and from scanning cross-sectional synchrotron high energy micro-X-ray diffraction (CSmicroXRD) with a spatial resolution of about ~20 μm are correlated. The novelty of the work resides (i) in introducing synchrotron CSmicroXRD methodology, based on *transmission diffraction geometry*, which allows for a simultaneous analysis of stress, microstructure and phase depth-gradients in the direct space, (ii) in applying robust complementary characterization approaches to assess cross-sectional structure-property relationships at the microscale and (iii) in observing cross-sectional correlations within the three different model sample systems. In contrast to previous studies dealing with relatively thin samples of ~50 μm in the X-ray beam direction [18–20], the current work focuses on the simultaneous characterization of gradients of phases, residual stresses and microstructure in bulk samples with the thickness of ~2 mm. Moreover, the three case hardened steel samples were selected without an additional intention to perform a further correlation between them.

2. Material and methods

2.1. Sample preparation

Three different martensitic steel samples were characterized in the present study: (i) a plasma-nitrided plate, (ii) a carburized cylinder and (iii) a shot-peened disc. The nominal compositions of the individual steel grades taken from [21–23] are given in Table 1. Each of the samples was surface modified as described below.

The *nitrided sample* was produced from a 30 × 30 × 10 mm^3 specimen of high alloy hot work steel type X38CrMoV5-1 (EN 1.2343 ESU – voestalpine Böhler Edelstahl GmbH, Kapfenberg, Austria) with a chromium content of 5%. The surface was modified by a long time low pressure plasma nitriding process. The sample was therefore kept in a process

Table 1 – Nominal chemical compositions of steel grades used for gas-nitriding, carburizing and shot-peening according to references [21–23], respectively. The particular alloying contents are given in wt.%.

Process/Steel Grade	C	Si	Mn	Cr	Mo	Ni	V	other
Nitriding/X38CrMoV5-1 – W300	0.39	0.97	0.43	5.0	1.14	0.21	0.35	
Carburizing/18CrNiMo7-6	0.17	0.25	0.50	1.65	0.3	1.55		Pb
Shot-Peening/41SiNICrMoV7-6 – 300M	0.42	1.65	0.8	0.8	0.3	1.8	0.8	

atmosphere of N_2, H_2 and Ar gas mixture for 28 h at a temperature of 510 ± 10 °C. The base material was initially gas-quenched after austenitization at ~1010 °C and tempered at 550, 530 and 520 °C during the first tempering, the second tempering to working hardness and the third tempering for stress relief, respectively. The temperature was held for ~90 min during each tempering step before the material was cooled to ambient conditions.

The *carburized specimen*, a cylinder with a diameter of 40 mm and a height of 25 mm of a low alloy case hardening steel type 18CrNiMo7-6 (EN 1.6857 – Deutsche Edelstahlwerke DEW, Witten, Germany), was case-hardened in an industrial vacuum furnace with dimensions of 0.6 × 0.75 × 1 m^3 by ALD Vakuum Technologies (Hanau, Germany). To enable the carbon enrichment in the near-surface region, the sample was low-pressure carburized for ~60 min in a hydrocarbon atmosphere (p = 10 mbar) at a temperature of ~960 °C. A martensitic microstructure was formed by high-pressure gas quenching using nitrogen with a pressure of ~10 bar. Finally, the sample was tempered at ~170 °C for ~90 min.

The *shot-peened specimen* is a precipitation hardened, high strength heat treatable steel disc (similar to type 41SiNiCrMoV7-6 – EN 1.6928 – voestalpine Böhler Edelstahl GmbH, Kapfenberg, Austria) with a dimension of 50 × 7 mm^2 (diameter × height). Before the peening process, the sample was hardened at 870 °C, quenched and double-tempered at 390 and 180 °C for 60 and 180 min, respectively. The surface hardness of the steel disc before peening was determined to be 563 HV_{10}. The specimen was shot-peened with an Almen-intensity of 0.2 ± 0.05 mmA [24] in the next step. Spherical steel powder with an initial diameter of ~0.35 mm was used as blasting material. To end up in a smooth surface topology, the sample was furthermore fine-peened with an Almen-intensity of 0.1 ± 0.05 mmA. The degree of coverage was 200% in both peening-process steps.

2.2. *Experimental methods*

For the CSmicroXRD analysis, steel platelets of ~(15 × 5 × 2) mm^3 were extracted from the three samples by precision cutting with an Accutom-5 (Struers, Germany) cutting machine, equipped with a diamond cutting wheel. A detailed analysis of near-surface residual stress relaxation caused by the sample cutting is discussed in Sec. 2.4 and in [18]. CSmicroXRD analysis was performed at the high energy materials science beamline P07B at the storage ring PETRAIII of DESY (German synchrotron) in Hamburg [25] in transmission diffraction geometry. The energy of the monochromatic beam was set to 87.1 keV which corresponds to a wavelength of 14.24 pm. Fig. 1 gives a schematic representation of the experimental setup with the beam penetrating a sample in transmission diffraction geometry. An experimental protocol of the used setup is presented in the supplementary data, Fig. S1. The near-surface regions of the three steel samples were scanned approximately at their centres by using a collimated pencil beam with a height and width of ~500 and ~20 μm, respectively, oriented parallel to the sample's surfaces (*cf.* Fig. 1), using a scanning increment of ~10 μm. A two-dimensional (2D) amorphous silicon digital X ray detector (model XRD1621 by PerkinElmer) with 2048 × 2048 pixels and a pixel pitch of 200 μm was used to collect the diffracted signal. LaB_6 standard was used to determine the sample-to-detector distance of ~1329 mm.

Each sample was aligned using a photo-sensitive diode and exact positions of the surfaces were determined in the same way.

OM of all samples was performed using an Olympus BX51 microscope equipped with an Olympus digital camera.

SEM images were recorded with a Gemini field-emission SEM equipped with double condenser optics (Carl Zeiss SMT, Oberkochen, Germany) operating at an accelerating voltages of 5 kV and a beam current of 10 nA. To secure a clean surface, the near-surface cross-section of the plasma-nitrided and carburized steel samples were, additionally to standard metallurgical preparation techniques (grinding, polishing), prepared by Ar^+ ion slicing at an ion milling system IM4000 (Hitachi High-Tech Corporation, Tokyo, Japan) using an accelerating voltage of 6 kV. N and C gradients in the parabola-shaped polished cross-sections of the plasma nitrided and carburized sample, respectively, were characterized by electron probe micro analysis (EPMA) using a X-Max 20 silicon drift detector by Oxford Instruments, suited for energy dispersive X-ray spectroscopy (EDX).

For the carburized sample, the cross-sectional C-profile was furthermore evaluated using an electron probe micro-analyser, type JEOL JXA-8200 "Superprobe", equipped with a wavelength dispersive spectrometer (WD-S). The setup was calibrated using a pure graphite calibrant before the polished metallurgical cross-section of the carburized sample was scanned by an electron beam of 15 kV acceleration voltage and 10 nA beam current with steps of 10 μm. The FWHM for each spot and the corresponding background were measured for 20 and 10 s, respectively.

Micro hardness measurement scans using a Vickers indenter were performed across the polished cross-sections using a Mitutoyo/Buehler Micromet 5104 testing device equipped with a digital camera and the commercial Buehler Omnimet analysing software. Test loads of 100 and 500 g_f, corresponding to $HV_{0.1}$ and $HV_{0.5}$, were used to indent the metallographic sections of the three samples at depths between 0 and 100 μm and at greater depths, respectively. Hardness values were calculated by averaging the result of

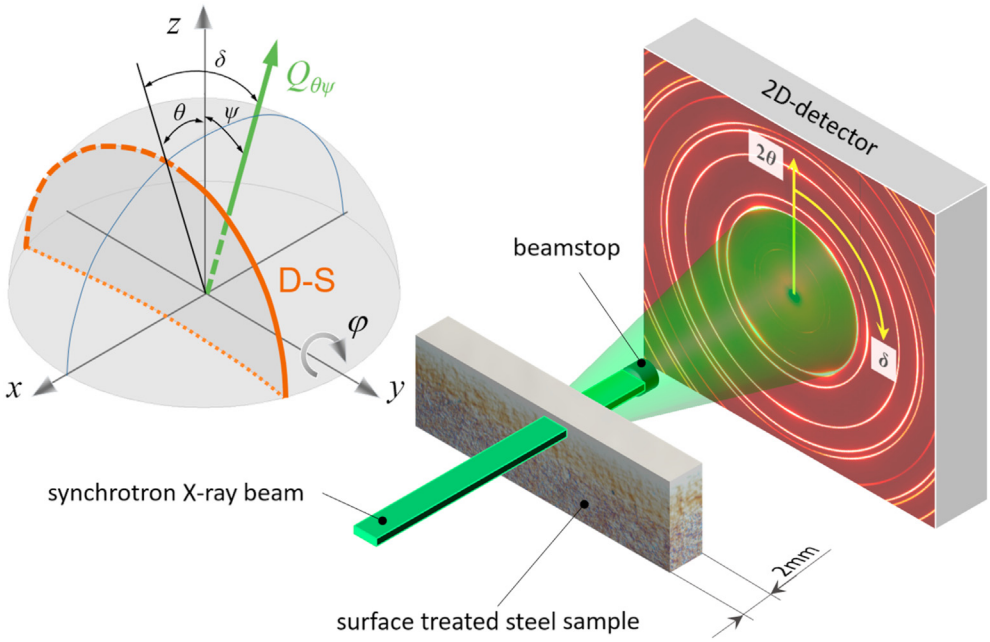

Fig. 1 – A schematic non-proportional drawing of the CSmicroXRD setup at the PETRA III synchrotron. The steel sample with a thickness of ~2 mm (in the beam direction) is moved along the z-direction in increments of ~20 μm. The sample surface is aligned parallel to the pencil beam by an ϕ rotation. The 2D detector collects a set of Debye–Scherrer (D–S) rings for each sample position using an acquisition rate of ~2 s/frame. The stereographic projection illustrates the projection of one single D–S ring with a particular corresponding diffraction vector $Q_{\theta\psi}$ schematically. The intensities of D–S rings at the azimuthal positions of $\delta = 0^\circ$ and 90° represent diffraction on crystallographic planes oriented approximately parallel and perpendicular to the sample surface, respectively. The angle ψ denotes the angle between $Q_{\theta\psi}$ and the normal of the surface of the sample z.

three indents at redundant depth positions. The experiments were performed following the guidelines of DIN EN ISO 6507 1:2006. Consequently, the minimum distance between two indents as well as minimum distances to boarders were taken into account. To determine the depth that was influenced by the nitriding and carburizing process, experimental HV data was fitted using an exponential decay function for the data down to a depth position of 600 μm. The core hardness value of the basic material was determined by averaging HV-values measured from 600 to 5000 μm.

2.3. CSmicroXRD data evaluation procedure

2D diffraction data (Fig. 1) were processed using the Python software package pyFAI [26]. The diffraction vector $Q_{\theta\psi}$ orientation-dependent lattice spacings $d_{\theta\delta}(z)$ were evaluated from Debye–Scherrer (D-S) rings recorded at particular Bragg's angles θ, the azimuthal angle δ and the samples' depths z (Fig. 1). To elucidate $d_{\theta\delta}(z)$-values, 36 D-S rings sections, each encompassing ~10° azimuthal range, were integrated and then evaluated using the Bragg's law. In general, D-S rings contain information on the crystallographic texture, the apparent size of coherently diffracting domains convoluted with the strains of second and third order (micro-strains), X-ray elastic strain of the first order (macro-strain) and volume fractions of phases within the irradiated gauge volume. Exact positions of the reflections' maxima as well as peaks' widths were fitted using a Pseudo-Voigt function. The novelty of this work resides mainly in the simultaneous examination of all above mentioned parameters using high-energy CSmicroXRD in bulk samples with a thickness of several mm, compared to the microscopic samples analysed in our previous studies [18–20].

X-ray elastic residual strain gradients at the particular sample depths z (Fig. 1) were determined from the D-S rings' ellipticity as follows

$$\varepsilon_{\theta\delta}^{hkl}(z) = \frac{d_{\theta\delta}^{hkl}(z) - d_0}{d_0} \quad (1)$$

with $d_{\theta\delta}^{hkl}(z)$ being the distorted lattice parameter due to elastic residual strains in the material and d_0 denoting the unstressed lattice parameter. It was assumed, that the three surface treatments had a negligible impact on the Poisson's ratio of the impacted materials. Therefore, depth-dependent unstressed lattice parameters d_0 (z) were calculated from the measured θ_0^{hkl} (z) positions of the diffraction peaks, which were retrieved (for each particular sample) from D–S rings always at the same rings' azimuthal position δ_0, representing the stress-free direction (cf. Fig. 1) [18,27].

Since the initial geometry of the samples was rotationally symmetric, it was approximated that in plane $\varepsilon_{11}(z) = \varepsilon_{22}(z) = \varepsilon(z)$ and out of plane $\varepsilon_{33}(z)$ strain components are dominant and the shear strain components $\varepsilon_{ij}(z)$ can be neglected for simplicity [18,28]. $\varepsilon_{22}(z)$ and $\varepsilon_{33}(z)$ components

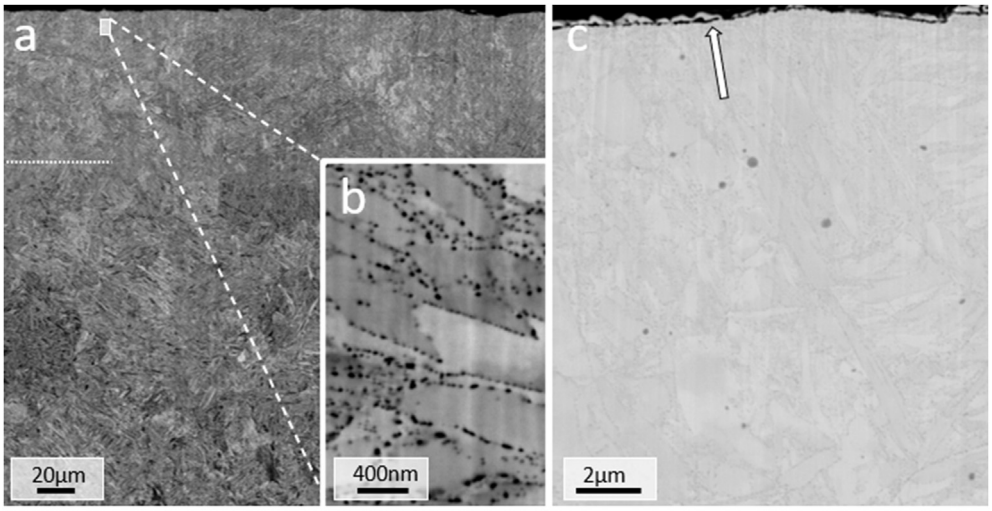

Fig. 2 – SEM-micrograph of the plasma-nitrided steel sample (a). The diffusion zone extends to a depth of ~80 µm (indicated by a white dotted line). The morphology of the precipitates is different in the diffusion zone and in the unnitrided core material. In the diffusion zone equiaxed interlath precipitates with a size of several tens of nanometers can be resolved (b) [36,37]. The presence of a discontinuous compound layer with a thickness of some tens of nanometers is indicated by an arrow and microscopic carbo-nitro precipitates are visible as equiaxed dark spots (c).

represent the strain along y and z axes, further denoted as "in-plane" and "out-of-plane" components, respectively. $\varepsilon_{11}(z)$ denotes the strain component in x direction (Fig. 1).

According to [29], intensities $I(\delta, z)$ recorded at particular D-S azimuthal positions δ (Fig. 1) can be transformed to $I(\psi, z)$ dependencies as follows

$$\cos\psi = \cos\delta\cos\theta \tag{2}$$

The linearity of experimentally determined $d_{\theta\delta}^{hkl}$ as a function of $\sin^2\psi$ values along the investigated depth was used to prove the validity of the applied evaluation method, especially the absence of shear strain and stress components [18]. Additionally, an equibiaxial stress state with $\sigma_{11}(z) = \sigma_{22}(z)$, $\sigma_{12}(z) \cong 0$ and $\sigma_{i3}(z) = 0\ (i = 1, 2, 3)$ at the samples' free surfaces can be assumed, whereas at greater depths the out-of-plane residual stress component $\sigma_{33}(z)$ cannot always be considered to be negligible [28,30,31]. Consequently, the distortion of the D-S rings as a function of the sample's depth can be generally expressed as follows

$$\frac{\partial d(\delta, z)}{\partial \sin^2\delta} = [\sigma_{22}(z) - \sigma_{33}(z)]\frac{1}{2}S_2^{hkl}d_0(z) \tag{3}$$

where $\frac{1}{2}S_2{}^{hkl}$ represents an X-ray elastic constant and d_0 the unstrained lattice parameter [18,32]. In the case of martensite (α'-Fe) and retained austenite (γ-Fe), X-ray elastic constants $\frac{1}{2}S_2^{211} = 6.304 \times 10^{-6}$ and $\frac{1}{2}S_2^{311} = 6.535 \times 10^{-6}$ MPa^{-1}, respectively, were estimated using the Kroener grain interaction model [28,33]. In other words, knowing the X-ray elastic constants of a material, one can determine the actual experimental (*Exp*) (residual) stress $\sigma_{22}(z) - \sigma_{33}(z)$ within the gauge volume from the slope of the linear regression in the $d_{\theta\delta}^{hkl}$ $-\sin^2\psi$ diagram, Eq. (3), as derived in [28]. Additionally, unstressed lattice parameters $d_0(z)$ can be simultaneously determined from the same system of linear equations in Eq. (3), considering the stress free direction defined by the azimuthal angle δ_0 [27,28]. In contrast to the experiments performed in laboratory conditions, d_0 and stresses can thus be elucidated directly from the D-S rings for every particular gauge volume without a previous knowledge of $d_0(z)$, as generally accepted. A detailed derivation of the stress evaluation procedure from two-dimensional synchrotron XRD data is presented elsewhere [18,20,27].

The actual angular resolution of the used setup is predetermined by the pixel size of 200 µm of the 2D detector, which corresponds to a 2θ angular range of ~0.0104° at $2\theta = 5°$ and at the sample-detector distance of 1329 mm. Exact positions of the diffraction angles in the three experiments were determined by a fitting algorithm in pyFAI. Peak widths (full-width-at-half-maximum (FWHM) values) were extracted from these fits. Deviations for strain (and stress) were calculated based on a Gaussian error propagation.

The volume fraction of γ-Fe within the α'-Fe matrix was determined by following an approach based on the ASTM practice E975-13 [34]. Accordingly, α'-Fe 200/002 and 112/211 doublets and the 200 and 220 reflections from γ-Fe were azimuthally integrated from $0 < \delta < 360°$. The presence of a crystallographic texture of the samples was assessed by evaluating the azimuthal distributions of the diffraction intensities $I(\delta,z)$ of the particular D-S-rings, as presented in the supplementary data (Figs. S3, S9, S12).

2.4. *FEM-modelling*

A finite elements model (FEM) was developed to reconstruct the original stress gradients within the three samples before cutting. As input parameters, the stress profiles $\sigma_{22}(z) - \sigma_{33}(z)$ in Eq. (3) determined experimentally by CSmicroXRD, samples' elastic constants and geometry were used. For this reason, a linear elastic material model using the pairs of

Young's moduli and Poisson's ratios of 215 GPa and 0.3, 190 GPa and 0.29 and 205 GPa and 0.28 was applied to the nitrided, carburized and shot-peened steels, respectively. Depending on the shape and dimensions of the three investigated samples, between 270000 and 660000 hexahedron elements with linear shape functions and reduced integration were used. In the samples' regions with stress gradients, structured meshes with element sizes of about 10 μm were built. Towards the outer region of the specimens the mesh size increased gradually up to an element size of about 3 mm. The model's symmetry was used to reduce the number of elements. The independence of the results on mesh size and element's aspect ratio was verified in a mesh convergence study.

In order to reconstruct the residual stress gradients across the uncut specimens a reverse engineering process was implemented. An initial stress state was therefore applied on the whole specimen, the cut was simulated by an element deletion of all elements except for the remaining sample geometry. The relaxed stresses of the simulated samples were analysed at the centre of the samples with respect to its x-dimension (Fig. 1). A mean stress throughout the sample's thickness was then calculated for each depth position and sample [18]. Finally, the modelled stress profiles $\sigma_{22}(z) - \sigma_{33}(z)$ denoted further as "FEM" stresses were optimized to fit the measured stress profiles from Eq. (3), further denoted as "Exp" stresses. The modelled residual stress gradients are presented together with the experimental results in Figs. 3–5 for comparison. Sample images with calculated stress distributions $\sigma_{22}(z) - \sigma_{33}(z)$ and stress relaxation tendencies are presented in the supplementary data (Figs. S7, S11, S13). The above residual stress reconstruction procedure was applied only to the stress profiles obtained from α'-Fe phase. For the γ-Fe phase, the approach was not applied because of the large standard deviations obtained for the experimental residual stress data.

3. Results

Cross-sectional data are presented on the basis of three case studies, each one for (i) the plasma nitriding, (ii) the carburizing and (iii) the shot-peening sample treatment.

3.1. *Case study I: low-pressure plasma nitrided hot work steel sample*

OM and SEM analyses were used to characterize cross-sectional microstructure of the plasma-nitrided X38CrMoV5-1 steel (type W300). The near-surface diffusion zone and the martensitic core material are presented in the cross-sectional SEM micrograph of Fig. 2a. The presence of a thin, discontinuous compound layer with an average thickness of less than 100 nm can be identified at the surface in Fig. 2c. The diffusion zone encompasses ~80 μm. The steel microstructure and the morphology of the precipitates change gradually across this region. Fig. 2b indicates the homogenous distribution of equiaxed dispersoids with a size of several tens of nanometres at the martensite interlath positions within the diffusion zone. Further SEM micrographs with different magnifications are presented in the supplementary data (Figs. S4, S5, S6). The analysis revealed that additional larger precipitates are present, out of which some are globular and others are elongated in shape.

The formation of the *nanoscopic precipitates* in Fig. 2b can be interpreted by transformation kinetics as discussed in [35–37]. Lerchbacher et al. [35] reported on the formation of retained γ-Fe films in quenched W300 hot work steel at martensite interlath boundaries. Mesquita et al. [36] investigated carbide precipitation as a function of various silicon contents in similarly alloyed hot work tool steels. Investigated alloy compositions, comparable to the steel grade of the present work, exhibited a formation of chromium-rich M_7C_3 coarser carbides, containing proportions of iron, molybdenum and vanadium that were also concentrated along martensite laths and packages boundaries. Michaud et al. [37] studied carbide formation in differently alloyed 5% Cr martensitic steels and observed the interlath precipitation of vanadium MC-carbides, chromium M_7C_3-and $M_{23}C_6$ carbides as well as iron M_3C carbides during tempering. Considering the findings from [35–37], it is assumed that the precipitates within the diffusion zone in Fig. 2b are mainly nitrides and carbonitrides formed at martensite interlath positions and former boundaries of austenite grains. Furthermore, carbo-nitro precipitates, visible in Fig. 2c (and in the supplementary data Figs. S3 – S5) as equiaxed and elongated dark spots, are secondary carbides precipitated from the tetragonally distorted as-quenched α'-Fe during the tempering treatments as well as carbides which had not been fully dissolved during austenitization.

In Fig. 3, cumulative results obtained using cross-sectional experimental techniques are presented. A depth profile of the Vickers hardness (superimposed on an OM micrograph in Fig. 3a) indicates a steep hardness decrease from ~1054 to a core hardness of ~589 $HV_{0.5}$, which is a typical value for this type of quenched and multiple-tempered steel grade [21]. The effective hardening depth can be determined at ~190 μm, meaning that the Vickers hardness at this position is 50 HV higher than the core hardness value.

CSmicroXRD analysis revealed austenite reflections, denoted as γ-Fe *hkl*, besides a dominant occurrence of martensite with pronounced α'-Fe *hkl* reflections, which are indexed as doublets in Fig. 3b. A formation of a thin compound layer with a thickness of less than 100 nm at the sample's surface (*cf.* Fig. 2c) could not be resolved by CSmicroXRD. Additionally, no diffraction signals from nitride and carbide precipitates could be observed within the diffusion zone and within the core material, respectively. The very weak signals at 2θ positions of 4.9, 5.3, 5.7° and 6.4 and 6.7° visible in Fig. 2b (logarithmic scale) can be attributed to α'-Fe and γ-Fe reflections, respectively, caused by high order harmonics of the synchrotron beam. If the synchrotron beam-energy is set by a crystal monochromator and no harmonic rejection optics is installed (like in the optics hutch at P07B), higher harmonics of the wavelength fulfilling Bragg's law with a higher order reflection, can pass through the crystal monochromator. Thus, additional peaks can appear in the XRD patterns, like in Fig. 2b.

In Fig. 3e and f, depth-dependent evolutions of the α'-Fe 112/211 reflection doublet for in-plane and out-of-plane diffraction vector orientations, respectively, are presented

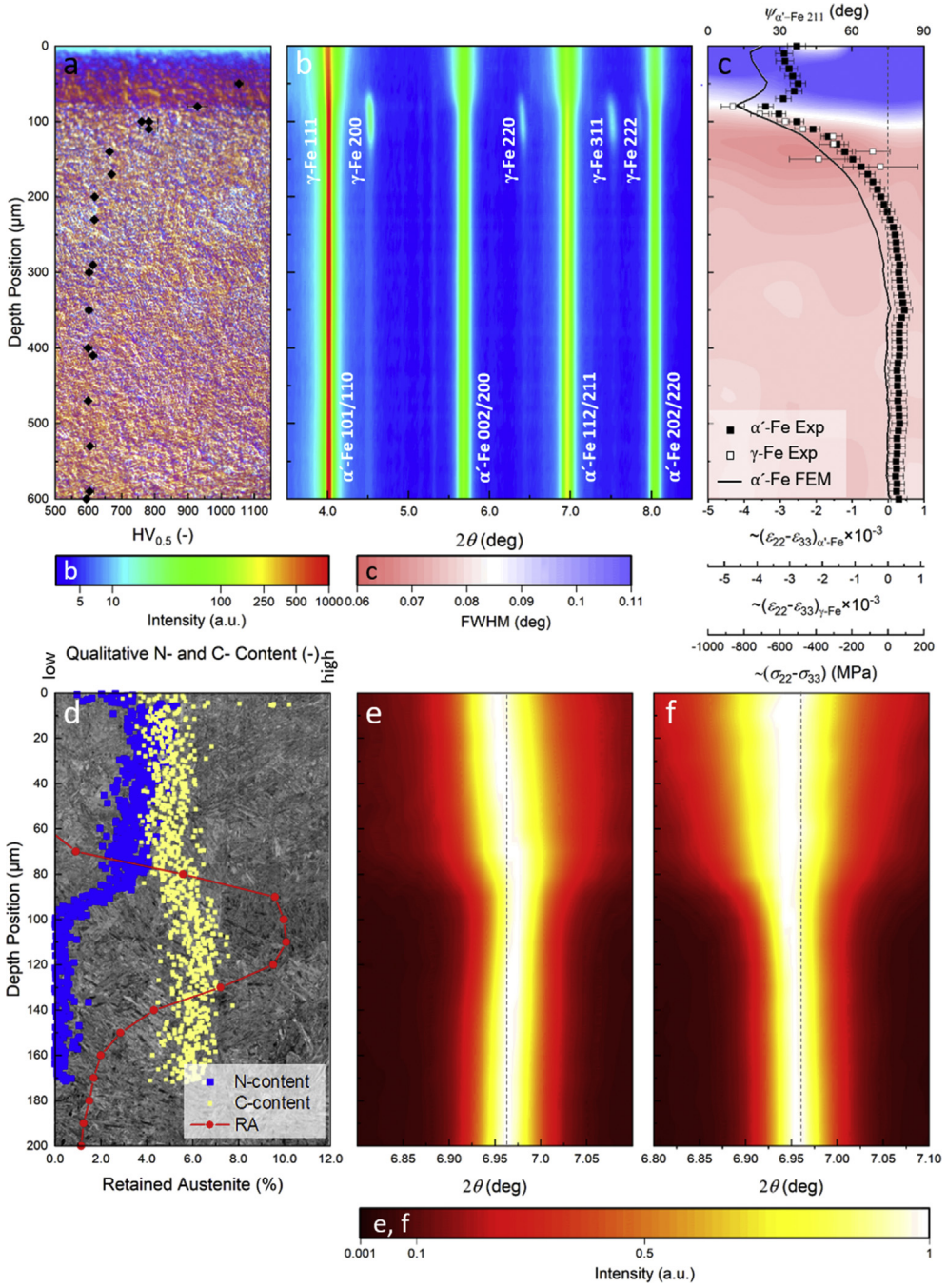

Fig. 3 – Correlative cross-sectional analysis of the low-pressure plasma nitrided steel sample. As indicated in the OM micrograph (a), the Vickers hardness decrease across the N-diffusion zone correlates with a gradual change in the near-surface martensitic microstructure (cf. also Fig. 2). The CSmicroXRD phase plot (b) indicates the presence of α'-Fe matrix and reverted γ-Fe at the interface between the N-diffusion zone and the martensitic core material. Not indexed, weak reflections at 2θ positions of 4.9, 5.3, 5.7° and 6.4 and 6.7° are α'-Fe and γ-Fe reflections, respectively, of higher order harmonics. (c) Experimental (Exp) and modelled (FEM) residual stress data representing $\sigma_{22}(z) - \sigma_{33}(z)$ stresses indicate compressive stress maxima at the edge of the diffusion zone in α'-Fe and γ-Fe phases, which can be correlated with the occurrence of reverted γ-Fe. A superimposed 2D map in (c) shows the FWHM distribution of the α'-Fe 220/202 reflection for various diffraction vector orientations ψ (cf. Fig. 1). The reverted γ-Fe occurrence at the bottom of the diffusion zone (d) correlates well with the C and N concentrations as well as the microstructure does. Gradual changes of FWHMs and positions of α'-Fe 112/211 reflections for in-plane (e) and out-of-plane (f) $Q_{\theta\psi}$ orientations originates from the presence of the residual stress gradient (c) and the modified microstructure (d).

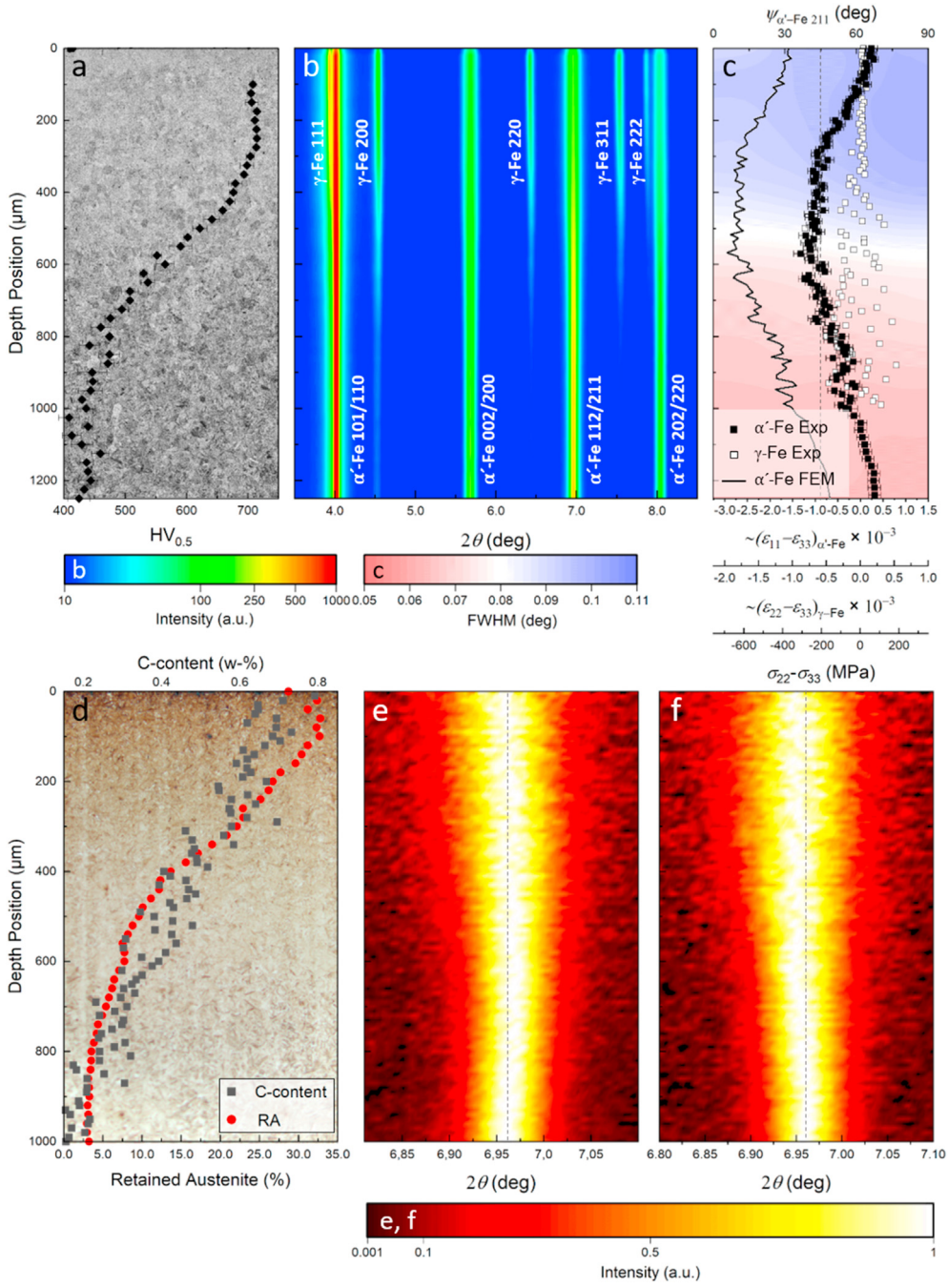

Fig. 4 – Cross-sectional analysis of the carburized steel sample. The analysis revealed a decreasing hardness and the gradient microstructure of the iron-martensite matrix along the sample's depth (a). The particular reflection intensities in the phase plot (b) indicate the presence of the dominant martensite matrix and a gradual decrease of retained γ-Fe volume fraction. The formation of residual stresses with a compressive stress peak of~−682 MPa in α'-Fe and negligible stresses in γ-Fe phase are visible in the modelled and experimental stress data in (c). Quantitative retained γ-Fe analysis correlates with the distribution of C down to the 1000 µm depth, which are shown in (d), together with the optical micrograph of the etched sample cross-section. The positions and FWHMs of α'-Fe 112/211 reflections in for in-plane (e) and out-of-plane (f) $Q_{\theta\psi}$ orientation change due to the compressive residual stress state in the carburized zone and microstructural refinement.

in detail. In general, one can observe an increase in the FWHMs at depths of 0–80 µm, which can be interpreted as the presence of micro-strain as well as by the crystallite size refinement induced by the increased N-concentration, as disclosed in Fig. 3d. The depth-dependent differences in the positions of the α'-Fe 112/211 doublet for in-plane and out-of-plane diffraction vector orientations (Fig. 3e and f) are, however, correlated to both, the crystal lattice expansion as well as by the presence of a residual stress gradient (Fig. 3c).

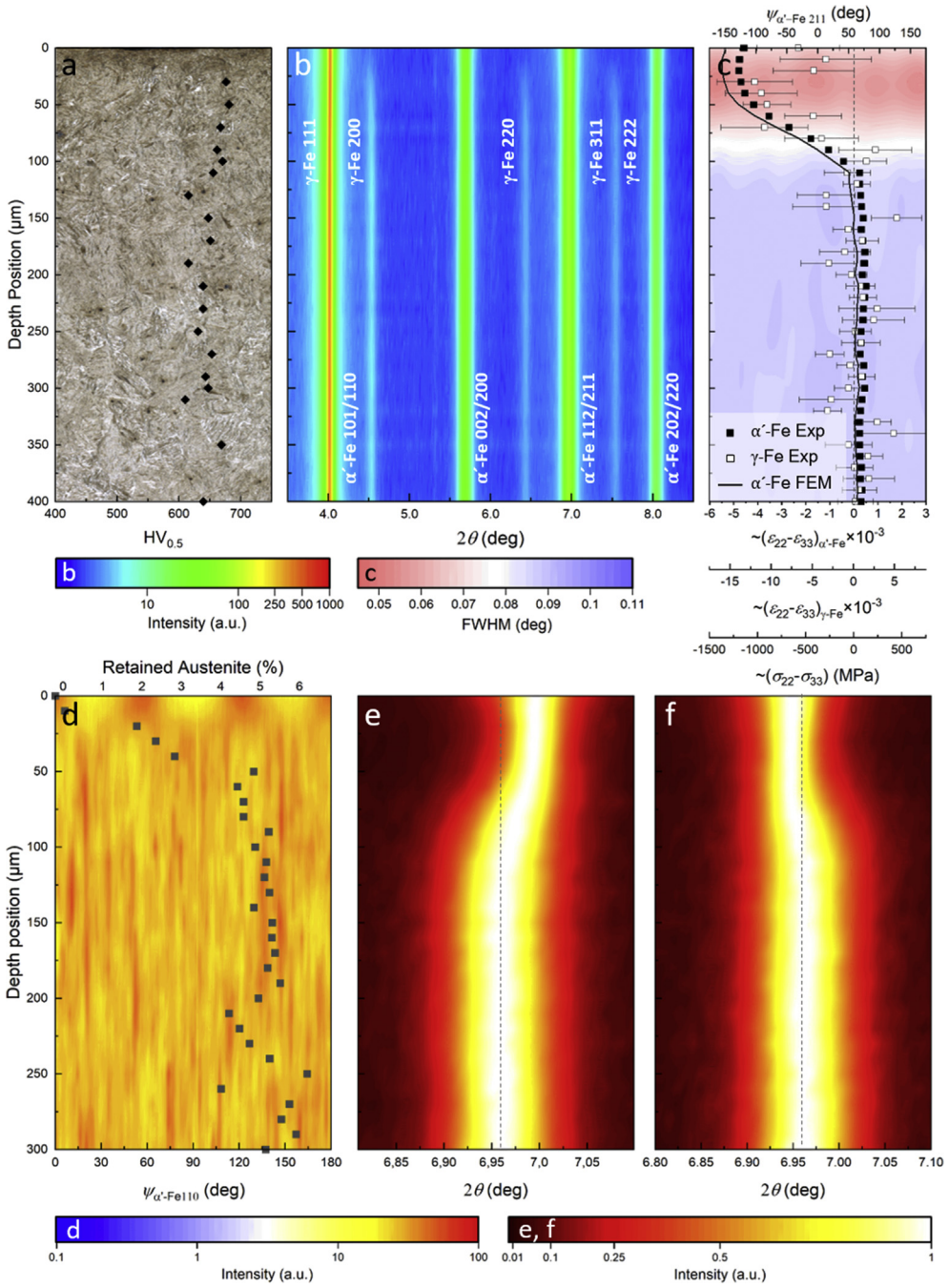

Fig. 5 – Cross-sectional analysis of the shot-peened sample. The investigations revealed a hardness increase toward the surface due to the work hardening effect that correlates well with the gradual change in the microstructure visible in the OM micrograph (a). The phase plot (b) confirms the presence of plastic strain induced phase transformation of the metastable γ-Fe to martensite in the shot-peening influenced near-surface region. A decrease in α'-Fe 112/211 FWHMs within the near-surface region (c) indicates that the shot-peening induced a significant rearrangement of the microstructure with larger crystallites and/or a lower density of structural defects, in agreement with the α'-Fe 112/211 profiles form (e) and (f) for in-plane and out-of-plane $Q_{\theta\psi}$ orientations, respectively. The quantitative γ-Fe analysis (d) exhibits a significant drop in the deformed region down to ~50 μm depth. Furthermore, the influence of the shot-peening treatment is shown by a <110> fibre texture formation down to ~20 μm depth in (d).

The γ-Fe reflections can be observed up to a depth of ~90 μm and a quantitative depth distribution of γ-Fe, estimated according to [34], is presented in Fig. 3d. The volume fraction of γ-Fe increases from 0 to ~9.58% within ~25 μm, starting ~65 μm below the surface and reaches a maximum of ~10.0% a depth of ~110 μm.

In Fig. 3c, a FWHM evolution of the α'-Fe 202/220 reflection as a function of the diffraction vector orientation ψ from the

range of ~(2.8–90)° (*cf.* Fig. 1) and the sample depth z is presented. The ψ angles of 2.8 and 90° represent approximately in-plane and out-of-plane orientations of the diffraction vector $\mathbf{Q}_{\theta\psi}$, respectively (Fig. 1). Additional information on the evolutions of α'-Fe FWHM as a function of sample's depth positions for the 101/110, the 002/200 and the 112/211 reflections are presented in the supplementary data (Fig. S2). In agreement with the data from Fig. 3e,f, the near-surface α'-Fe 202/220 reflection broadening in Fig. 3c can be correlated with the domain size and micro-strain increase [38], which can be further correlated with the presence of the N-diffusion zone visible in Fig. 3d.

Superimposed on the FWHM map in Fig. 3c, experimental and modelled residual stress gradient data differing up to 20% are presented. In α'-Fe, two compressive (FEM) stress maxima of~−765 and ~−841 MPa at depths of ~10 and ~80 μm can be identified, respectively. A steep stress relaxation can further be observed at a depth of ~230 μm. The high near-surface stresses are mechanically balanced by low tensile stresses, which are present at larger sample depths. Fig. 3c also shows the stress distribution within the γ-Fe phase, which correlates well with the level of the α'-Fe. Since the corresponding measurement errors of the evaluated stresses for the γ-Fe phase are inversely proportional to its volume fractions, they can be effectively compared with those from α'-Fe only at the depth of 80–150 μm, where the γ-Fe concentration is relatively high. The origins of the compressive stress maxima in both phases are discussed below.

Residual stress profiles in α'-Fe and γ-Fe can be correlated to the depth distributions of N and C in the near-surface region (Fig. 3d) as well as with the microstructural refinement manifested by the FWHM increase (Fig. 3c, e, f), the phase evolution and here, particularly, the local occurrence of γ-Fe (Fig. 3b). Within the first ~4 μm below the surface, N- and C-contents are complementary reduced and elevated, respectively. Below, they remain relatively stable and further decrease to zero and slightly increase, respectively, at the depth of 83 μm, the edge of the diffusion zone.

The chemical composition profile of carbon can be used to interpret the formation of two compressive residual stress peaks in Fig. 3c. During plasma-nitriding, N diffuses into the near-surface area and causes a redistribution of the C throughout and also underneath the diffusion zone. Furthermore, C is firstly being partially exchanged by nitrogen in precipitates, especially in Cr, M_7C_3-type carbides and secondly being redistributed throughout the diffusion zone. The formation of a compound layer at the surface is documented to act as a diffusion barrier for C [39]. As a result of the C-diffusion, the EPMA-profile (Fig. 3d) exhibits a C-peak at a depth of ~5 μm and a C-enriched zone at the edge of the diffusion zone. Comparable results during plasma nitriding of steel are presented and discussed in [39,40]. The localized increase in the concentrations of N and C is assumed to expand the α'-Fe lattice, which results in a formation of stress at a depth of ~83 μm.

Additionally, the increased C content at the front of the N-diffusion zone, which is the interface between the diffusion zone and the unnitrided core material (Fig. 3d), is assumed not only to contribute to a localized stabilisation of the γ-Fe phase but also to a localized reversion of α'-Fe to γ-Fe during the long-term plasma nitriding. To the best authors knowledge, this effect has not been reported before on a W300 steel grade. Typically, austenite reverse transformation can be observed in quench and partitioning (Q&P) steels [41]. Raabe et al. [42] documented on a phase transformation of α'-Fe to γ-Fe at grain boundaries in a Fe-9 at.% Mn and a Fe-12 at.% Mn maraging steel during aging at 450 °C. In that case, the localized reversion of α'-Fe to γ-Fe was correlated with the segregation of Mn at α'-Fe interlath boundaries. Jegou et al. [43] determined a coarsening of pre-existing carbides in a ferrite matrix at the nitriding front in differently nitrided Fe-3.5Cr-0.35C (wt.%) model-steel but no reversion of α'-Fe to γ-Fe in their samples. No coarsening of pre-existing carbides could be documented in this sample (supplementary data, Fig. S6). Thus, we assume that not the locally elevated C content itself but the combination of a locally elevated C content, the α'-Fe matrix and the simultaneous presence of Si in the W300 causes the localized reversion of α'-Fe to γ-Fe.

The exact origin, the formation kinetics and the character of the reverted γ-Fe build up (Fig. 3b) in the nitrided W300 steel however needs to be further investigated.

Complementary experimental results from CSmicroXRD and other techniques presented in Figs. 2 and 3 can be correlated. The thickness of the diffusion zone revealed quantitatively by EDX (*cf.* Fig. 3d) correlates (i) with the morphological changes in the microstructure in Fig. 2, (ii) with the broadening of martensite reflections from Fig. 3b,c,e,f and (iii) with the presence of compressive stresses in Fig. 3c. Additionally, two compressive residual stress maxima in Fig. 3c can be correlated with the increased concentration of N and C interstitial atoms (*cf.* Fig. 3d) and also with the local occurrence of reverted γ-Fe at the depth of ~80 μm (Fig. 3a). At greater depths, residual stress distribution can be correlated also with the hardness profile in Fig. 3a: compressive stress relaxes at ~230 μm, which is the same position where the value of the core hardness was measured.

There were several attempts to assess cross-sectional structure-property relationships in plasma-nitrided W300 steel samples. Leskovsek et al. [10] studied the correlation of residual stress (assessed by the hole drilling method) and micro-hardness gradients within eight differently plasma nitrided W300 samples. Similar to the results of the present work, they reported on the correlation between residual stress and micro-hardness gradients and suggested a routine to estimate residual stresses from a hardness-related parameter. It is notable, that they could not observe the formation of a compound layer at plasma-nitriding temperatures of 480° but just 60 °C above, at a temperature of 540 °C, which is in contradiction with the compound layer build-up at 510 °C in the present work. Remarkably, residual stress profiles obtained by hole drilling [10] are comparable to the results of the present work in terms of their shape and maximal compressive stresses of ~−700 to −850 MPa. However, two stress maxima (Fig. 3c) as well as a coexistence of α'-Fe and γ-Fe were not reported. Similar, Kurz et al. [3] reported on depth gradients of residual stresses, unstressed lattice parameters, microstructure and the N-diffusion during gas nitriding of Fe-M(= Al, V) specimens. High-energy synchrotron X-ray diffraction was employed to assess the spatially resolved stress state which was correlated to different precipitation

mechanisms. Due to the small beam size of 20 × 5 μm^2 (horizontal × vertical) that was used in their setup, the nitrided samples were moved parallel to the cross-sectional surface along the y-direction to obtain more representative diffraction data at specific sample depths.

3.2. *Case study II: low-pressure carburized case-hardening steel sample*

The CSmicroXRD approach was additionally applied to a carburized case-hardened steel sample (Fig. 1). A SEM micrograph in Fig. 4a obtained from the cross-section of the carburized 18CrNiMo7-6 steel indicates a gradual morphological change across the martensite matrix and a decreasing volume fraction of the (brighter) γ-Fe phase as a function of the sample depth (also visible in the high-resolution SEM images presented in the supplementary data Fig. S8). For this sample, the cross-sectional changes in the microstructure (Fig. 4a) and phase (Fig. 4b) evolutions can be correlated as well with the distribution of C diffused into the near-surface region, as presented in Fig. 4d and in supplementary data Fig. S10b. Superimposed on the SEM micrograph, Fig. 4a also shows the hardness depth-profile across the diffusion zone and the core material. Vickers hardness measurements revealed a case hardness of 711 ± 5 $HV_{0.5}$, which is almost constant down to the depth of ~275 μm. Further below, the hardness decreases gradually to a core hardness of ~431 ± 13 $HV_{0.5}$ observed at a depth of ~800 μm. According to EN ISO 2639, the case hardening depth (CHD) of carburized samples is defined as the depth, at which the hardness reaches the limit of 550 HV_1. In this case, the CHD of the sample was determined for ~660 μm below the surface. The corresponding hardness profile is presented in the supplementary data (Fig. S10a).

The cross-sectional phase analysis indicates gradual changes in the volume fractions of the α'-Fe matrix and the γ-Fe fraction (Fig. 4b), which were observed priorly by SEM (Fig. 4a). In the near surface area at a depth smaller than ~600 μm, broadened α'-Fe *hkl* and retained γ-Fe *hkl* reflections are pronounced due to the high C-content (Fig. 4d). At depths greater than ~250 μm, the decreasing volume fraction of γ-Fe is reflected by a decreasing intensity of the γ-Fe reflections while the intensity of the martensite peaks increases and their FWHM decreases, because of the supposed ceasing tetragonal distortion of martensite.

The FWHM evolution of the α'-Fe112/211 reflection as a function of the diffraction vector orientation ψ and the sample depth position is presented in Fig. 3c. A notable increase in martensite's FWHM down to a depth of ~580 μm (*cf.* Fig. 4e and f) correlates (i) with the observed $CHD_{HV0.5}$ (using a test load 500 g_f – *cf.* Fig. 4a) and (ii) with the maximum of the compressive residual stress of ~−682 MPa from the FEM model. In the carburized sample, the difference between experimental and modelled stresses is large (*cf.* Fig. 4c). This effect is caused by the comparable dimensions of the carburized sample depth of ~1 mm, the stress-affected region of more than 2 mm and the sample thickness in the *x* direction of 2 mm. This effect was extensively discussed in [18]. The distribution of the residual stresses and the reversal of compressive to tensile stresses at ~80 μm depth can again be correlated to the C-content and to the increasing volume fraction of γ-Fe. A second reversal in sign of the residual stresses occurs at a depth of ~1030 μm. As a consequence of mechanical equilibrium, tensile stresses are induced at depths above and below these positions, respectively. Residual stresses in γ-Fe are low compared to α'-Fe (Fig. 4c) but display a significantly higher variance. Their nature down to a depth of ~300 μm is tensile. A similar observation for γ-Fe was also reported by Ericsson et al. [17]. In α'-Fe phase, the stress profile originates from quenching and from martensite phase transformation hardening, the latter one depending strongly on the C-content. It should be noted that the martensite start temperature (M_s) as well as the yield stress are being attained at different locations of the sample at different times during quenching [15,17].

The specific stress gradient formed during quenching in Fig. 4c can be interpreted by considering segments of the hardening process and their corresponding sample depth dependent transformation kinetics, described in detail in [15,17].

The gradual change of the martensite start (and finish) temperature as a function of the C-content furthermore affects the quantity of retained γ-Fe. Fig. 4d presents a quantitative depth distribution of the retained γ-Fe. Within the first 100 μm below the surface, a high γ-Fe volume fraction of ~31.7% could be evaluated, which decreases gradually to the magnitude of 2.8% within the core material at 800 μm and below.

Fig. 4e and f shows the α'-Fe 112/211 reflection evolution for $\mathbf{Q}_{\theta\psi}$ in-plane and out-of-plane orientation, respectively, down to the sample depth of 1000 μm. The intensities occurring at both $\mathbf{Q}_{\theta\psi}$ orientations were normalized frame per frame to the individual maximal intensity of the reflection. The shift and the broadening of the reflections at depths of ~(0–800) μm can be correlated to the compressive residual stress increase and to the unstressed lattice parameter increase, due to interstitially soluted C. The maximum peak shift can be observed at ~580 μm depth, which is the depth of the highest compressive stress magnitude (Fig. 4c) and the $CHD_{HV0.5}$ that was determined with a test load of 500 g_f (Fig. 4a).

3.3. *Case study III: shot-peened martensitic steel sample*

The CSmicroXRD approach was additionally applied to a shot-peened martensitic steel. The microstructure, the hardness profile and the distributions of the phases and residual stresses of the shot-peened hardened and double-tempered 300M steel sample are presented in Fig. 5.

The darker appearance of the microstructure down to the depth of ~20 μm in the Nital-etched cross-section (Fig. 5a) is caused by the absence of retained γ-Fe in this area. In the same region, the shot peening treatment attained a strain induced phase transformation from γ-Fe to α'-Fe. The effect of a strain-induced transformation of retained γ-Fe into α'-Fe during shot-peening was documented also by Ebenau et al. [8]. Their study reports that a shot-peening treatment of austempered nodular cast iron samples with high volume fractions of up to ~19 and ~39% γ-Fe resulted in a significant reduction of the γ-Fe content and a formation of α'-Fe at depths down to ~300 μm.

In Fig. 5, the microstructure changes gradually to the tempered α'-Fe base material with increasing depth. In the uninfluenced core, a γ-Fe volume fraction of ~5% could be evaluated (Fig. 5d), whereby Vicker's hardness values decrease simultaneously from ~694.5 ± 5 $HV_{0.5}$ at ~50 μm to ~663 ± 10 $HV_{0.5}$ at ~170 μm (Fig. 5a), which is the depth that corresponds to the uninfluenced base material.

CSmicroXRD indicates the presence of a dominant martensite matrix with a small volume fraction of γ-Fe in the unpeened base material (Fig. 5b). A quantitative γ-Fe analysis (Fig. 5d), revealed a steep γ-Fe decrease at depths smaller than ~50 μm whereas an amount of ~5% could be determined in the unpeened material.

The decrease in the martensite's FWHM values in the deformed region for the α'-Fe 112/211 reflection is presented in Fig. 5c and can be interpreted as follows: (i) due to the massive plastic deformation induced by the shot-peening process, grain orientations of the initially untextured material were rearranged in order to form a <110>-fibre-texture within the influenced regions (*cf.* Fig 5d and Fig. S12 in the supplementary data) and (ii) the energy impact due to the shot-peening process was high enough to increase the size of the coherently scattering domains and to decrease micro-strains at depths smaller than ~20 μm due to an annealing effect (*cf.* [6,7]).

The applied shot-peening treatment induced high compressive (FEM) stresses of ~−1371 MPa at the depth of 20 μm (Fig. 5c) in α'-Fe. As a result, a pronounced peak shift of the α'-Fe 211/112 doublet to higher and lower angles for in-plane and out-of-plane $Q_{\theta\psi}$ orientations, respectively, can be observed in Fig. 5e and f. The reversal in sign of the compressive residual stresses occurs at a depth of ~105 μm. At greater depths, negligible tensile stresses could be evaluated. Due to the weak intensities of γ-Fe phase D-S rings, the residual stress values in γ-Fe exhibit high standard-deviations, although the stress levels approach that of martensite (Fig. 5c).

The cumulative results in Fig. 5 obtained from various cross-sectional characterization techniques show remarkable correlations. At a depth of ~20 μm, down to which the modified microstructure due to deformation-induced phase transformation can be observed by OM (Fig. 5a), <110> fibre-texture formation (Fig. 5d and supplementary data, Fig. S12), an abrupt change in the FWHM evolution (Fig. 5c) and the compressive residual stress peak (Fig. 5c) were observed.

Scholtes and Vöhringer [7] discussed the influence of shot-peening and the peening parameters on the near-surface regions they describe a strain-induced transformation of retained γ-Fe and the evolution of a <110> fibre texture. Results obtained by CSmicroXRD in the present work coincide with these findings from hardened steels and document that the shot-peening process results not only in a surface plastification and stress formation but also in remarkable changes in the near-surface microstructure and the phase composition.

4. Discussion

This study demonstrates the advantages of applying synchrotron CSmicroXRD technique in conjunction with conventional laboratory techniques (like OM, SEM, EDX and micro-hardness profiling) to characterize gradients of residual stresses, microstructures, crystallites morphology, composition and hardness in surface treated steels. The main aim of the work is to show the possibilities of CSmicroXRD analysis on three different sample types, without any additional intention to carry out a further correlation between the samples and the results. The three samples were selected to test the CSmicroXRD approach. Consequently, hereafter methodological aspects of the results are discussed followed by only a few materials science related points.

In general, CSmicroXRD can be considered as an upscaling of X-ray nanodiffraction conducted using sub-50 nm X-ray beams usually on micro-lamellae of ~50 μm in thickness (in the X-ray beam direction) and of crystallite size of several tens of nanometers [19]. Due to the larger grain size of the steel samples (even in the micrometer range) and the larger depth of interest (in the millimeter range), it is reasonable to apply scanning high-energy X-ray microdiffraction (CSmicroXRD) to obtain both sufficient diffraction statistics and satisfactory depth resolution within relatively thick samples of several millimeters. Additionally, in comparison with the results presented in previous X-ray microdiffraction studies e.g. in [3], the present work indicates the possibility to evaluate not only residual stress gradients but also gradients of crystallographic texture, FWHM and crystalline phases from the 2D XRD data. In this way, complex correlations between the microstructure and stresses on one side and the applied process conditions as well as the functional properties, like gradients of hardness, on the other side can be deduced. It can be expected that the relatively simple CSmicroXRD setup (Fig. 1) will be used in future to routinely investigate surface-treated bulk samples by high energy X-ray diffraction.

The comparison of the modelled and experimental stress dependencies in Figs. 3–5 indicates reasonable differences up to ~15% in nitrided and shot-peened samples (Figs. 3c and 5c), due to the relatively small affected depths of the samples by both processes. In the case of carburized sample, the (experimental) stresses relaxed nearly by 50% in the cut sample (Fig. 4c). As already mentioned, this is caused by the comparable dimensions of the carburized sample depth of ~1 mm and the sample thickness in the x direction of 2 mm. This effect was studied and discussed in [18].

It is obvious, that absolute magnitudes of the residual stresses (in Figs. 3c, 4c and 5c) obtained from the three investigated specimens cannot be directly compared due to the different alloying concepts and surface treatments of the steel grades. It follows, that the use of particular X-ray elastic constant ½ $S_2 = (1 + \nu)/E$ provide not absolute but just approximate residual stress values. An experimental study of Marion and Cohen [44] indicated, that individual X-ray elastic constants should be individually, experimentally determined in principle not only for different steel compositions but also for different grain sizes, microstructures, deformations and heat treatments. Consequently in the present case, X-ray elastic constants should be determined for every sample depth and the corresponding material composition and microstructure. This has not been done in this work, thus, resulting imprecisions were taken in account during the error determination. Therefore, the residual stress data in Figs. 3c,

4c and 5c are presented together with experimentally determined X-ray elastic strains.

The experimental results from the three different surface-treated steel samples (Figs. 3–5) allows to draw conclusions on the near-surface gradients and their correlations. However, since the steel grades used for the individual experiments differ one from another, it is not trivial or it could even be impossible to draw significant correlations between the experimental data from Figs. 3–5. In the low-pressure plasma-nitrided hot-work tool steel W300 (Fig. 3), a local occurrence of γ-Fe at depths greater than ~80 μm was detected by CSmicroXRD. On the one hand, the heat treatment introduced in [21] indicates a full transformation from retained γ-Fe to α'-Fe during or after the three tempering cycles. Hence, the presence of γ-Fe prior to the nitriding process can be excluded in the present case. On the other hand, the Fe–C–N phase diagram indicates that the formation of γ-Fe below 590 °C should not be possible, as well as during the nitriding process at 510 °C in the present case. *Jegou* et al. [43] investigated the role of C-diffusion and its impact on the development of residual stresses in differently nitrided ferritic model alloy Fe–3Cr–0.35C (wt.%) samples. A growth of the carbide particles ahead of the nitriding front but no α'-Fe-to γ-Fe reversion from was documented in their work. In contrast to the model alloy used in [43], W300 contains a significant higher content of ~1.1 wt.% Si [21]. Therefore, the origin of γ-Fe in Fig. 3 is assumed to be correlated with the segregation of γ-Fe stabilizing elements, probably C, at α'-Fe interlath boundaries in combination with an increased Si-content during the 28 h low-pressure plasma nitriding at 510 °C. Due to a higher defect density in the (initial) martensitic microstructure of the W300, the diffusivity of interstitial elements is expected to be higher here compared to a ferrite. Additionally, it is worth mentioning that standard laboratory XRD investigations could easily miss the presence of this reverted γ-Fe phase as they are performed at the surface of the sample in reflection geometry.

Based on the previous aspect, it should be noted, that the origins of γ-Fe formation in the plasma-nitrided W300 steel grade (section 3.1, Fig. 3) and in the low-pressure carburized case hardening steel 18CrNiMo7-6 (section 3.2, Fig. 4) are assumed not to be the same. The gradual formation of *retained* γ-Fe in the carburized case-hardened steel can be attributed to the elemental C-profile in Fig. 4d and can be understood by the resulting time- and chemistry-dependent reception of the α'-Fe temperature M_s. In contrast, in the nitrided sample both, mainly interstitial C and substitutional Mn as well as Si, are assumed to contribute to the localized occurrence and stabilization of *reverted* γ-Fe.

In the carburized sample, however, a discrepancy in the macro-stress formation was observed for α'-Fe and γ-Fe phases (Fig. 4c). This effect can be explained as follows: In contrast to the nitrided and the shot-peened samples – which do not exhibit a comparable discrepancy (cf. Fig. 3c and 5c) – the carburized sample was tempered at 170 °C for ~90 min (section 2.1). During this additional tempering cycle α'-Fe and γ-Fe phases were heated up and expanded. Taking in account a surface carbon content of ~0.67 at.% (Fig. 4d and Fig. S10b), linear thermal expansion coefficients for γ-Fe and α'-Fe can be estimated according to [45], as ~24.6 × 10^{-6} and 13.6 × 10^{-6} K^{-1}, respectively. This means that the γ-Fe would expand almost twice as much as the α'-Fe matrix but as the expansion is supressed by the (harder) matrix, γ-Fe is compressively stressed. Once the yield strength of (the softer) γ-Fe is exceeded, the γ-Fe phase deforms plastically. Consequently, tensile stresses occur in the γ-Fe phase after the final cooling of the material.

5. Summary and conclusions

This methodological study introduces correlative cross-sectional micro-analytics based primarily on the application of scanning high-energy synchrotron CSmicroXRD analysis of phases, residual stresses and microstructure, performed in combination with other conventional characterization technologies (like optical and electron microscopy, HV-analysis and electron probe microanalysis). The approach was used to reveal complex structure-property gradients in near-surface regions of three model surface-treated steels. In the technology of surface-treated steel products, the correlative approach and the possibilities of CSmicroXRD will represent an important tool to understand the complex correlations between the applied surface treatment process parameters, the fabricated near-surface gradients and the parts' overall mechanical properties.

This correlative approach was applied to three representative model sample systems. The particular materials science findings of the CSmicroXRD, OM, SEM, micro-HV-profiling and electron probe microanalyses are shortly summarized hereafter.

The near-surface diffusion of N into the plasma-nitrided W300 surface gives rise to a gradual distribution of nitrides and morphological changes in martensite matrix within the ~80 μm thick diffusion zone (Fig. 3). A residual stress profile with two local compressive maxima of ~765 and ~841 MPa was elucidated and correlates well with the N and C distributions as well as with the resulting width of the diffusion zone, the local occurrence of γ-Fe and the microstructural changes (Fig. 3). The second residual stress maximum can be correlated with the γ-Fe occurrence at the front of the N-diffusion zone.

The case hardening depth in a low-pressure carburized 18CrNiMo7-6 steel sample could be correlated with the occurrence of a compressive residual stress peak of ~682 MPa (Fig. 4). Again, the diffusion profile of C, obtained by wavelength dispersive X-ray spectroscopy, is related to the gradual change of the retained γ-Fe volume fraction in the near-surface region.

A massive plastic deformation induced by the shot-peening in the near-surface region down to ~25 μm caused a formation of a <110>-fibre texture within an initially untextured quenched and tempered 300M steel (Fig. 5). Shot-peening furthermore led to a localized significant decrease in γ-Fe caused by a plastic-strain induced transformation into martensite as well as to the formation of high compressive residual stresses with a stress maximum of ~1371 MPa–25 μm below the surface.

Finally, the work shows that CSmicroXRD in combination with standard laboratory characterization techniques represent a powerful tool to determine complex structure-property

correlations within the near-surface regions of mechanically and thermo-chemically treated steels. Cross-sectional investigation of the near-surface regions is essential for the understanding of the complex chemical and physical processes occurring in the steels during the surface treatments and can subsequently be used to optimize the particular process recipes.

Declaration of Competing Interest

The authors declare that they have no known competing financial interests or personal relationships that could have appeared to influence the work reported in this paper.

Acknowledgements

A part of this work was supported by Österreichische Forschungsförderungsgesellschaft mbH (FFG), Project No. 861496, "CrossSurfaceMech". Financial support by the Austrian Federal Government (in particular from Bundesministerium für Verkehr, Innovation und Technologie and Bundesministerium für Wissenschaft, Forschung und Wirtschaft) represented by Österreichische Forschungsförderungsgesellschaft mbH and the Styrian and the Tyrolean Provincial Government, represented by Steirische Wirtschaftsförderungsgesellschaft mbH and Standortagentur Tirol, within the framework of the COMET Funding Programme is gratefully acknowledged. Part of the research leading to this result has been supported by the project CALIPSOplus under the Grant Agreement 730872 from the EU Framework Programme for Research and Innovation HORIZON 2020.

Appendix A. Supplementary data

Supplementary data to this article can be found online at https://doi.org/10.1016/j.jmrt.2021.01.099.

Author's contributions

S.C.B. performed the XRD experiments at DESY, analysed and interpreted the data from various experimental techniques, visualized the results and coordinated the experimental activities. M.M. supported the XRD experiments at DESY and contributed to the XRD data interpretation. T.Z. performed laboratory experiments on the carburized sample and interpreted these data. H.W. developed the thermo-chemical treatments of the low-pressure plasma nitrided and carburized steels and provided the samples. C.S. developed the peening process and provided the sample. T.H. established the funding of the collaborative research, contributed to the project conceptualization and the project administration. B.S. carried out the EDX analyses in the SEM. W.E. and M.K. developed and performed the FEM model simulation on residual stresses. N.S. developed the XRD setup and supported the experiments at DESY. J.K. established the funding of the collaborative research, made the project conceptualization and the project administration, organized and coordinated resources and experimental activities. S.C.B. and J.K. wrote the original draft of the manuscript, reviewed and edited it and coordinated the contribution of all other authors.

REFERENCES

[1] Schneider MJ, Company TT, Chatterjee MS. Introduction to surface hardening of steels[1]. Stell Heat Treat Fund Process 2018;4:389–98. https://doi.org/10.31399/asm.hb.v04a.a0005771.

[2] Kratzer D, Dobler F, Tobie T, Hoja T, Steinbacher M, Stahl K. Effects of low-temperature treatments on surface hardness, retained austenite content, residual stress condition and the resulting tooth root bending strength of case-hardened 18CrNiMo7-6 gears. Proc IME C J Mech Eng Sci 2019;233:7350–7. https://doi.org/10.1177/0954406219846160.

[3] Kurz SJB, Meka SR, Schell N, Ecker W, Keckes J, Mittemeijer EJ. Residual stress and microstructure depth gradients in nitrided iron-based alloys revealed by dynamical cross-sectional transmission X-ray microdiffraction. Acta Mater 2015;87:100–10. https://doi.org/10.1016/j.actamat.2014.12.048.

[4] Gibmeier J, Rebelo-Kornmeier J, Strauss T. Local residual stress depth distribution in the inner gearing of a case hardened sliding collar. Mater Sci Forum 2016;879:601–6. https://doi.org/10.4028/www.scientific.net/msf.879.601.

[5] Benedetti M, Fontanari V, Ho B. Influence of shot peening on bending tooth fatigue limit of case hardened gears. Int J Fatig 2002;24(11):1127–36. https://doi.org/10.1016/S0142-1123(02)00034-8.

[6] Nordin E, Alfredsson B. Experimental investigation of shot peening on case hardened SS2506 gear steel. Exp Tech 2017;41(6):433–51. https://doi.org/10.1007/s40799-017-0183-4.

[7] Scholtes B, Vöhringer O. Ursachen, Ermittlung und Bewertung von Randschichtveränderungen durch Kugelstrahlen. Materialwissenschaft Und Werkstofftechnik; 1993. https://doi.org/10.1002/mawe.19930241206.

[8] Ebenau A, Lohe D, Vohringer O, Macherauch E. Influence of shot peening on the microstructure and the bending fatigue strength of bainitic-austenitic nodular cast iron. In: ICSP, vol. 4. The Japan Society of Precision Engineering; 1990. p. 389–98.

[9] Merkel J, Schulze V, Vohringer O. The effects of shot peening and deep rolling on the surface layer and the mechanical properties of sintered iron. In: Icsp-9, vol. 3; 2005. p. 241–6.

[10] Leskovšek V, Podgornik B, Nolan D. Modelling of residual stress profiles in plasma nitrided tool steel. Mater Char 2008;59:454–61. https://doi.org/10.1016/j.matchar.2007.03.009.

[11] Díaz-Guillén JC, Alvarez-Vera M, Díaz-Guillén JA, Acevedo-Davila JL, Naeem M, Hdz-García HM, et al. A hybrid plasma treatment of H13 tool steel by combining plasma nitriding and post-oxidation. J Mater Eng Perform 2018;27:6118–26. https://doi.org/10.1007/s11665-018-3669-z.

[12] Epp J, Hirsch T, Hunkel M, Wimpory RC. Combined neutron and X-ray diffraction analysis for the characterization of a case hardened disc. Mater Sci Forum 2010;652:37–43. https://doi.org/10.4028/www.scientific.net/msf.652.37.

[13] Díaz NEV, Schacherl RE, Zagonel LF, Mittemeijer EJ. Influence of the microstructure on the residual stresses of nitrided iron-chromium alloys. Acta Mater 2008;56:1196–208. https://doi.org/10.1016/j.actamat.2007.11.012.

[14] Christiansen T, Somers MAJ. Avoiding ghost stress on reconstruction of stress- and composition-depth profiles from destructive X-ray diffraction depth profiling. Mater Sci Eng 2006;424:181–9. https://doi.org/10.1016/j.msea.2006.03.007.
[15] Ericsson T. In: Residual stresses produced by quenching of martensitic steels, vol. 12. Elsevier; 2014. https://doi.org/10.1016/B978-0-08-096532-1.01209-7.
[16] Prevéy PS. X-ray diffraction characterization of residual stresses produced by shot peening. Shot Peen Theor Appl 1990;c:81–93.
[17] Ericsson T. Residual stresses caused by thermal and thermochemical surface treatment 1987;2:31.
[18] Stefenelli M, Todt J, Riedl A, Ecker W, Müller T, Daniel R, et al. X-ray analysis of residual stress gradients in TiN coatings by a Laplace space approach and cross-sectional nanodiffraction: a critical comparison. J Appl Crystallogr 2013;46:1378–85. https://doi.org/10.1107/S0021889813019535.
[19] Stefenelli M, Daniel R, Ecker W, Kiener D, Todt J, Zeilinger A, et al. X-ray nanodiffraction reveals stress distribution across an indented multilayered CrN-Cr thin film. Acta Mater 2015;85:24–31. https://doi.org/10.1016/j.actamat.2014.11.011.
[20] Zeilinger A, Todt J, Krywka C, Müller M, Ecker W, Sartory B, et al. In-situ observation of cross-sectional microstructural changes and stress distributions in fracturing TiN thin film during nanoindentation. Sci Rep 2016;6:22670. https://doi.org/10.1038/srep22670.
[21] Medvedeva A, Andersson J, Robertsson R, Nilsson C, Ejnermark S. W300 - hot work tool steel, vol. 6; 2019.
[22] Deutsche-Edelstahlwerke. Carbodur 6587 - werkstoffdatenblat 18CrNiMo7-6, 1.6587. 2016.
[23] Böhler High Performance Metals International GmbH V. 300M - Böhler V132 data sheet. 2020. www.bohler.at/austria/de/products/v132/. [Accessed 28 March 2020].
[24] Almen JO, Black PH. Residual stresses and fatigue in metals. New York: McGraw-Hill; 1963.
[25] Schell N, King A, Beckmann F, Ruhnau HU, Kirchhof R, Kiehn R, et al. The high energy materials science beamline (HEMS) at PETRA III. AIP Conf Proc 2010;1234:391. https://doi.org/10.1063/1.3463221.
[26] Kieffer J, Karkoulis D. PyFAI, a versatile library for azimuthal regrouping. J Phys Conf 2013;425:202012. https://doi.org/10.1088/1742-6596/425/20/202012.
[27] Geandier G, Vautrot L, Denand B, Denis S. In situ stress tensor determination during phase transformation of a metal matrix composite by high-energy X-ray diffraction. Materials 2018;11:1–19. https://doi.org/10.3390/ma11081415.
[28] Noyan IC, Cohen JB. Residual stress - measurement by diffraction and interpretation. 1987. https://doi.org/10.1002/crat.2170240228.
[29] Heidelbach F, Riekel C, Wenk HR. Quantitative texture analysis of small domains with synchrotron radiation X-rays. J Appl Crystallogr 1999;32:841–9. https://doi.org/10.1107/S0021889899004999.
[30] Dölle H. The influence of multiaxial stress states, stress gradients and elastic anisotropy on the evaluation of (Residual) stresses by X-rays. J Appl Crystallogr 1979;12(6):489–501. https://doi.org/10.1107/S0021889879013169.
[31] Renault PO, Le Bourhis E, Villain P, Goudeau P, Badawi KF, Faurie D. Measurement of the elastic constants of textured anisotropic thin films from x-ray diffraction data. Appl Phys Lett 2003;83:473–5. https://doi.org/10.1063/1.1594280.
[32] Vermeulen AC. An elastic constants database and xec calculator for use in xrd residual stress analysis. Adv X Ray Anal 2001;44:128–33.
[33] Kim SA, Johnson WL. Elastic constants and internal friction of martensitic steel, ferritic-pearlitic steel, and α-iron. Mater Sci Eng 2007;452–453:633–9. https://doi.org/10.1016/j.msea.2006.11.147.
[34] ASTM International. Standard practice for X-ray determination of retained austenite in steel with near random crystallographic orientation 1. Astm; 2009. https://doi.org/10.1520/E0975-13.
[35] Lerchbacher C, Zinner S, Leitner H. Atom probe study of the carbon distribution in a hardened martensitic hot-work tool steel X38CrMoV5-1. Micron 2012;43:818–26. https://doi.org/10.1016/j.micron.2012.02.005.
[36] Mesquita RA, Barbosa CA, Morales EV, Kestenbach H-J. Effect of silicon on carbide precipitation after tempering of H11 hot work steels. Metall Mater Trans A 2011;42(2):461–72. https://doi.org/10.1007/s11661-010-0430-0.
[37] Michaud P, Delagnes D, Lamesle P, Mathon MH, Michaud P, Delagnes D, et al. The effect of the addition of alloying elements on carbide precipitation and mechanical properties in 5% chromium martensitic steels to cite this version : HAL Id : hal-01715082 the e ff ect of the addition of alloying elements on carbide precipitation a. 2019.
[38] Scherrer P. Bestimmung der Größe und der inneren Struktur von Kolloidteilchen mittels Röntgenstrahlen. In: Nachrichten von der Gesellschaft der Wissenschaften Zu Göttingen, Mathematisch-Physikalische Klasse. 2. Göttigen: Gesellschaft der Wissenschaften zu Göttingen; 1918. p. 98–100.
[39] Tier MA, Kieckow F, Strohaecker TR, Da Silva Rocha A, Bell T. A study of carbon redistribution during plasma nitriding of steel. In: Proceedings - 15th IFHTSE - international federation for heat treatment and surface engineering congress 2006; 2006. p. 193–9.
[40] Barrallier L. Classical nitriding of heat treatable steel. Woodhead Publishing Limited; 2015. https://doi.org/10.1533/9780857096524.3.393.
[41] Dieck S, Rosemann P, Kromm A, Halle T. Reversed austenite for enhancing ductility of martensitic stainless steel. IOP Conf Ser Mater Sci Eng 2017;755. https://doi.org/10.1088/1757-899X/181/1/012034.
[42] Raabe D, Sandlöbes S, Millán J, Ponge D, Assadi H, Herbig M, et al. Segregation engineering enables nanoscale martensite to austenite phase transformation at grain boundaries: a pathway to ductile martensite. Acta Mater 2013;61:6132–52. https://doi.org/10.1016/j.actamat.2013.06.055.
[43] Jegou S, Barrallier L, Kubler R, Somers MAJ. Evolution of residual stress in the diffusion zone of a model Fe-Cr-C alloy during nitriding. HTM - Haerterei-Technische Mitteilungen 2011;66:135–42. https://doi.org/10.3139/105.110104.
[44] Marion R, Cohen J. The need for experimentally determined X-ray elastic constants. Adv X Ray Anal 1976;20. https://doi.org/10.1154/S0376030800011964. Twenty-fifth annual conference on applications of X-ray analysis(13):355–367.
[45] Lee SJ, Lusk MT, Lee YK. Conversional model of transformation strain to phase fraction in low alloy steels. Acta Mater 2007;55:875–82. https://doi.org/10.1016/j.actamat.2006.09.008.